Geophysical Journal International

Geophys. J. Int. (2010) doi: 10.1111/j.1365-246X.2010.04587.x

Interpreting spatial variations in anisotropy: insights into the Main Ethiopian Rift from SKS waveform modelling

J. O. S. Hammond,[1] J.-M. Kendall,[1] D. Angus[1,2] and J. Wookey[1]

[1] *Department of Earth Sciences, University of Bristol, Wills Memorial Building, Queens Road, Bristol* BS8 1RJ, *UK. E-mail: j.hammond@bristol.ac.uk*
[2] *School of Earth and Environment, University of Leeds, Leeds* LS2 9JT, *UK*

Accepted 2010 March 4. Received 2010 March 4; in original form 2009 September 9

SUMMARY

Seismic anisotropy is a common feature in the upper mantle and measuring shear wave splitting in core phases is a common approach in estimating its characteristics. Large lateral variations in estimated splitting parameters are observed over small spatial distances in many differing tectonic regions, including areas of continental break-up such as the Main Ethiopian Rift (MER). We investigate the ability of shear wave splitting analysis to constrain spatial variations in anisotropy using a one-way wave equation modelling scheme to generate bandlimited waveforms for a suite of models representing regions with rapidly changing anisotropy. We show that shear wave splitting can identify lateral variation in anisotropy on the order of 20–50 km, where a change in fast direction demarcates the transition in anisotropy. In addition, variation in the amount of splitting is complicated close to the transition, and is sensitive to the vertical thickness of anisotropy. We have used these modelling results to interpret shear wave splitting measurements for the MER. The model that best fits the observations has a 100- km wide rift zone with a fast direction of 30° outside and 20° inside the rift. The model has 9 per cent anisotropy close to the western margin, with 7 per cent anisotropy elsewhere. In all regions of the model we constrain the anisotropy to begin at a depth of 90 km. The depth of anisotropy is consistent with geochemical estimates of the depth of melt initiation beneath the region. Also the elevated splitting beneath the western margin supports evidence of low velocities and highly conductive zones from seismic tomography and magneto-tellurics, suggesting melt is more focused along the western margin. This study shows how observations of *SKS*-wave splitting from dense seismic networks can be used to map sharp lateral changes and constrain the depth of the anisotropy.

Key words: Seismic anisotropy; Wave propagation; Continental tectonics: extensional; Africa.

1 INTRODUCTION

Seismic anisotropy can be described as the variation of seismic wave speed with direction of propagation. In most studies the main cause of anisotropy in the upper mantle is assumed to be the lattice preferred orientation (LPO) of olivine where the olivine fast axis (*a*-axis) aligns in the direction of upper-mantle flow (Babuska & Cara 1991; Mainprice *et al.* 2000). This could be caused by current mantle processes, or due to accumulated strain, which has 'frozen' in an anisotropic signature from previous deformation events. Other mechanisms that cause upper mantle anisotropy are fluid filled cracks (Crampin & Booth 1985) or the preferred orientation of inclusions (e.g. oriented melt pockets—OMP, see Kendall 1994; Blackman & Kendall 1997) mechanisms that can be very efficient at generating large amounts of anisotropy (Kendall 2000).

A common way of constraining anisotropy in the upper mantle is shear wave splitting analysis. When a shear wave enters an anisotropic medium it splits into two quasi-shear waves that are polarized orthogonally to each other and propagate with different velocities. These split shear waves can be used to characterize anisotropy in terms of an apparent symmetry axis (typically fast shear wave direction, ϕ) and the time-lag between fast and slow shear waves (δt, a proxy for amount, or extent of anisotropy).

Many studies investigating upper mantle anisotropy based on shear wave splitting utilize *SKS*-phases. This is a wave that travels as an *S* wave through the mantle and a *P* wave through the outer core. It is advantageous to use this phase because it is a clear arrival over a range of epicentral distances (85°–120°), making it observable in most regions. Also, it is possible to ignore source side anisotropy due to the fact that the seismic energy converts to a *P* wave at the core–mantle boundary (CMB), thus the measured anisotropy can be attributed to the mantle beneath the station. Another benefit is that the rays travel almost vertically in the uppermost mantle making *SKS*-wave splitting a useful tool to distinguish lateral variations in anisotropy (see Silver 1996; Savage 1999; Kendall 2000, for examples). However, due to the near vertical ray paths it is very hard to

© 2010 The Authors
Journal compilation © 2010 RAS

place any constraints on the depth extent of anisotropy, which has led to much debate on whether anisotropy can be attributed to lithospheric fabric [fossil anisotropy (Silver 1996), fluid filled cracks (Crampin & Booth 1985)], or asthenospheric processes [for example, flow at plate boundaries (Blackman & Kendall 2002), simple asthenospheric flow (Savage 1999), density driven flow (Behn *et al.* 2004)].

Some attempt has been made to constrain the depth extent of anisotropy based on consideration of *SKS* Fresnel zones (Alsina & Snieder 1995; Rümpker & Ryberg 2000). For instance, it can be assumed that two different splitting results from nearby stations indicate that the *SKS* waves are sampling different anisotropic regions. Thus, the depth of origin of the anisotropy can be estimated as anywhere shallower than the depth where the Fresnel zones beneath each station overlap. Favier & Chevrot (2003) and Chevrot *et al.* (2004) apply a finite-frequency Frechet derivative approach and calculate 3-D sensitivity kernels for shear wave splitting intensity, which are similar to those estimated from Fresnel zone estimates (Alsina & Snieder 1995; Rümpker & Ryberg 2000).

Other studies have utilized finite difference modelling schemes to investigate the ability of shear wave splitting to identify lateral and depth variations in anisotropy (e.g. Rümpker & Silver 2000), and have placed some constraints on the distribution of anisotropy beneath transform faults and shear zones (Rümpker *et al.* 2003; Chevrot 2006; Chevrot & Monteiller 2009) and a plume setting (Rümpker & Silver 2000). All these studies show that regions with laterally varying anisotropy give rise to complicated splitting measurements.

In this paper, we address the suitability of the *SKS*-wave splitting technique to constrain sharp lateral variations in anisotropy, and further investigate the ability of this seismological technique to constrain the depth extent of the anisotropy. This is done using a finite-frequency waveform modelling technique (Angus *et al.* 2004). This study improves on previous modelling of laterally varying anisotropy by providing some general guidelines that can be applied to shear wave splitting observations in regions with sharp lateral changes in anisotropy. This study was motivated by observations of *SKS*-wave splitting beneath the Main Ethiopian Rift (MER) (Kendall *et al.* 2005, 2006), and these results are used as a case study to highlight the utility of the modelling. This approach is applicable to any region that has sharp boundaries in anisotropy, such as transform faults or suture zones.

2 FINITE FREQUENCY WAVEFORM MODELLING

We construct synthetic seismograms using the one-way wave equation modelling scheme of Angus *et al.* (2004) and Angus & Thomson (2006), for waves propagating vertically through a medium containing OMP (Fig. 1). The model is constructed by calculating the elastic constants for vertically aligned melt pockets, using the approach of Hudson (1981) and applying these elastic constants at each node. The elastic constants are calculated using *P*- and *S*-wave velocities of 7.8 and 4.0 km s^{-1} (matrix material) and 2.5 and 0.0 km s^{-1} (crack material) and densities of 3.8 and 2.7 kg m^{-3} for the matrix material and crack material, respectively. The cracks consist of penny shaped inclusions with an aspect ratio of 0.01. Crack density is then varied to calculate elastic constants with varying magnitudes of anisotropy. We characterize this anisotropy in terms of maximum shear wave anisotropy (i.e. 10 per cent anisotropy refers to a maximum shear wave anisotropy of 10 per cent). Motivated by Kendall *et al.* (2005) a MER rift-like model is constructed (Fig. 1) (e.g. a rotated horizontal symmetry axis in the rift zone). The simulations are done in 3-D, but with only 2-D variations in anisotropy.

In the models the fast direction is oriented 30° from north outside the rift, and north–south inside the rift. An *SKS* like wave (i.e. small waveform curvature (4.2^{-12} s m^{-1}), 8 s period) is then propagated through the 3-D anisotropic model using the finite-difference one-way wave propagator formulation (Angus *et al.* 2004; Angus & Thomson 2006). There is a sharp transition between these two regions (i.e. gridpoints on either side of the transition between rift and flank have differing fast axis orientations and hence elastic constants). The one-way wave equation method models transmitted waves (it ignores backscattering which is not an issue in modelling *SKS*-wave arrivals), taking into account frequency dependent coupling effects due to, for instance, rapidly rotating wave polarization effects due to slowness surfaces (Crampin & Yedlin 1981).

All waves are Ricker wavelets (although wavelet type has no effect on the result), have a dominant period of 8 s (except model 6, where frequency dependence is investigated), and initial source polarisation of 45° (except model 7, where initial polarization dependence is investigated). The output waveforms are then analysed identically to the data (see Kendall *et al.* 2005), and the apparent splitting is estimated for a profile spanning the 'rift' zone. To estimate the splitting we use the Teanby *et al.* (2004) cluster analysis method which is based on the Silver & Chan (1991) method. This technique performs a grid search over δt and ϕ, rotating the horizontal components by ϕ, and shifting their relative positions by δt. The values of δt and ϕ which provide the most linear particle motion provides our estimate of the splitting. A statistical F-test is used to asses the uniqueness of the result, thus providing an error estimate. The observed splitting depends on several parameters (outlined in Table 1) and each parameter is studied in turn (Figs 2–6). Finally, based on the modelling results, the observed splitting parameters of Kendall *et al.* (2005) (Fig. 7) are modelled to place estimates on the anisotropic characteristics beneath the MER.

2.1 Model class 1: Varying width of 'rift' zone

The first variable tested is rift width (all other variables are held constant: maximum *S*-wave anisotropy = 10 per cent, depth of anisotropy = 45 km (from surface), dominant period = 8 s, initial polarization = 45°). We vary the width of the rift zone between 100 and 10 km (Fig. 2). A smooth transition in ϕ is seen for all rift widths. The inflexion point in the ϕ profile marks the boundary between anisotropic regions (Fig. 2). However, δt shows considerably more variation across the rift boundaries. The expected δt for this model is a constant value of 1.27 s, but we see large variations, similar to those seen for other studies of inhomogeneous anisotropic media [e.g. plume, Rümpker & Silver (2000); transform fault, Rümpker *et al.* (2003)].

2.2 Model class 2: varying magnitude of anisotropy

The second variable tested is the magnitude of anisotropy (all other parameters are held constant: rift width = 40 km, depth of anisotropy = 45 km (from surface), dominant period = 8 s, initial polarization = 45°). All models within this class show a smooth transition in ϕ, with the inflexion point showing the transition between anisotropic regions. The δt profile shows a similar trend for all models. The magnitude of splitting depends on the amount of anisotropy, but the peaks and troughs of the δt curve all lie in the same place (see Fig. 3).

© 2010 The Authors, *GJI*
Journal compilation © 2010 RAS

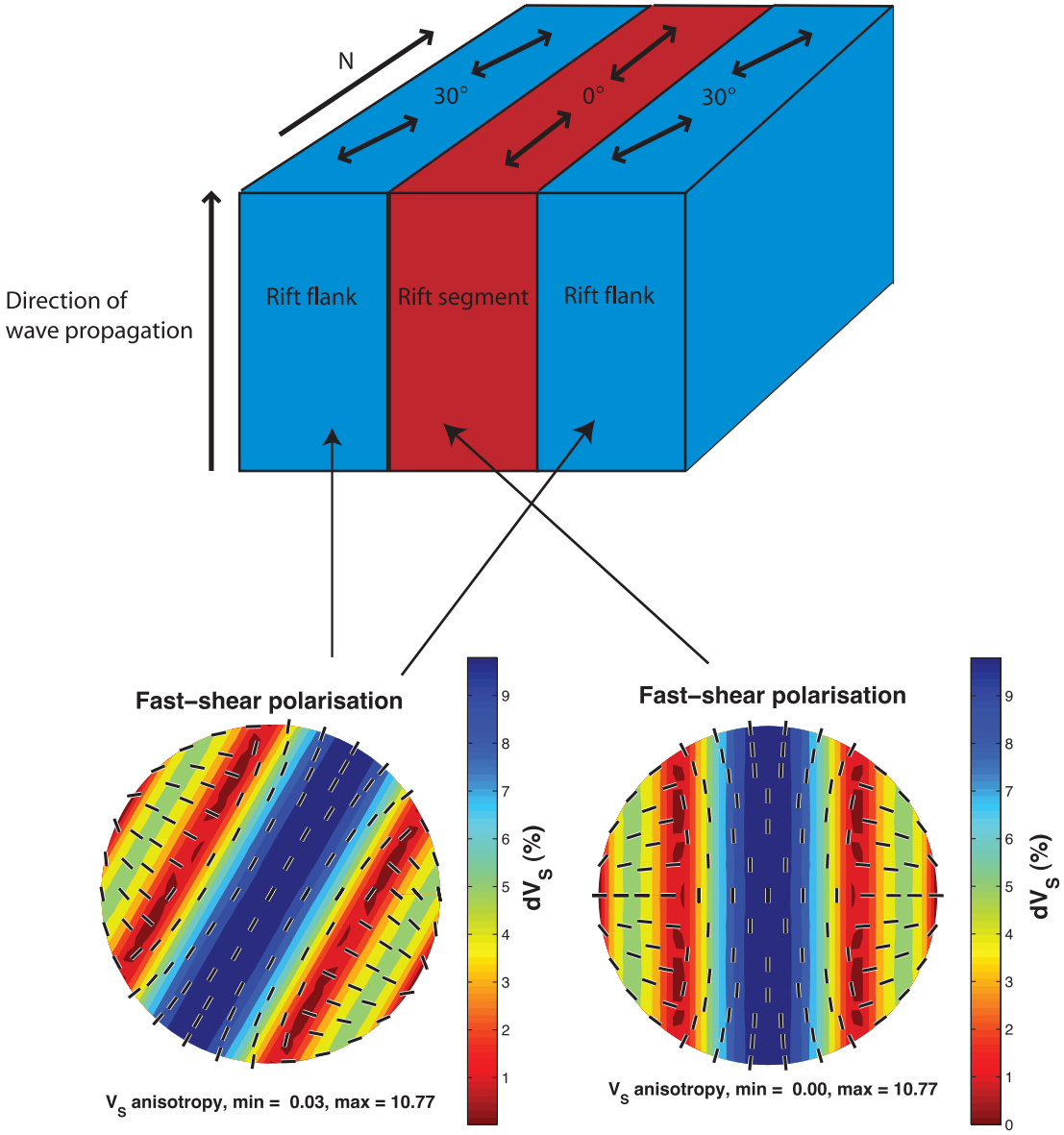

Figure 1. Top panel: a schematic representation of the model used in the one-way wave equation modelling scheme. Bottom panel: hemispherical projections of the elastic constants applied at each node. The colour scheme shows the variation of magnitude of shear wave anisotropy, and the black ticks show the fast direction of a wave propagating through the anisotropic medium, as a function of direction of propagation. Elastic constants are calculated for vertically aligned melt pockets using the approach of Hudson (1981), see text for details. For the modelling the symmetry plane on the rift flanks is oriented 30° from north, and in the rift segment it is oriented north–south. All other parameters (rift width, amount of anisotropy, depth extent of anisotropy, frequency of incoming wave and initial polarization of incoming wave), are varied systematically (Table 1) and results are displayed in Figs 2–6.

Table 1. Parameters tested in the various models.

Model number	Varying parameter	Range	Figure
1	Width of anisotropic zone	10–100 km	2
2	Magnitude of anisotropy	4–10 per cent	3
3	Depth extent of anisotropy	25–85 km	4
4	Dominant period of incoming wave	0.5–10 s	5
5	Initial polarization of incoming wave	15–165°	6

2.3 Model class 3: varying thickness of anisotropic zone

The third variable tested is depth (i.e. thickness from the surface) of the anisotropic zone (all other parameters are held constant: rift width = 40 km, maximum *S*-wave anisotropy = 10 per cent, dominant period = 8 s, initial polarization = 45°). The variation of ϕ is smooth for nearly all models in this class, with the inflexion point showing the transition between anisotropic regions. An exception occurs in the model with an 85-km-thick layer (Fig. 4). The variation in ϕ seen in the 85-km-thick layer has some deviation at the boundary between anisotropic regions. This may be due to multipathing effects; a result of the longer wave path through a complex,

© 2010 The Authors, *GJI*
Journal compilation © 2010 RAS

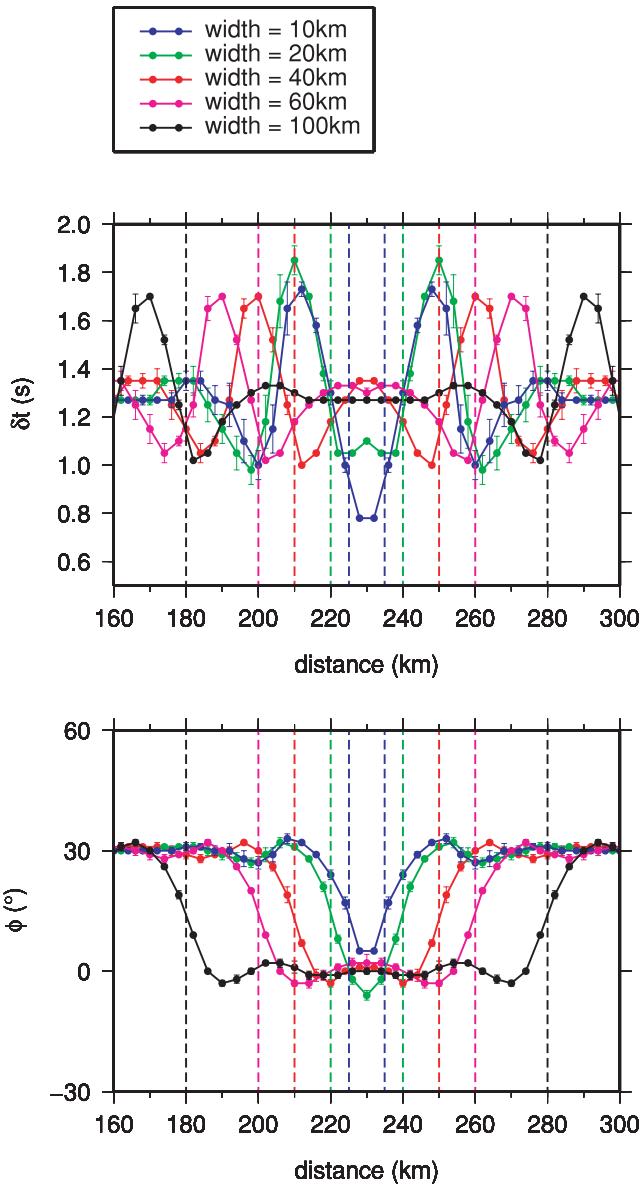

Figure 2. Model 1: varying rift width. Other parameters: maximum *S*-wave anisotropy = 10 per cent, anisotropic depth = 45 km, Period = 8 s, initial polarization = 45°. Coloured dashed lines indicate the rift width for each model. Note smooth transition in ϕ, with inflexion points marking rift width, and complicated variation of δt.

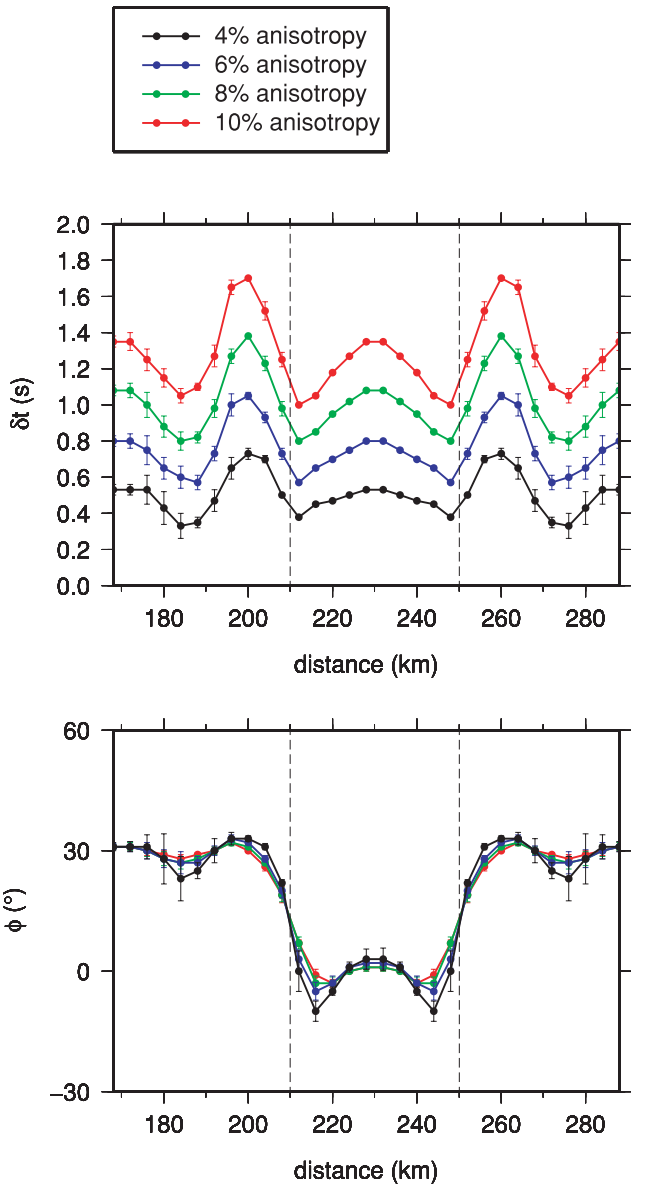

Figure 3. Model 2: varying maximum *S*-wave anisotropy. Other parameters: rift width = 40 km, anisotropic depth = 45 km, Period = 8 s, initial polarization = 45°. Black dashed line indicates the rift width for the model. Note similar curves to model 1, but with the δt varying proportionally to the amount of anisotropy. The peaks and troughs in the δt profile do not change with varying amounts of anisotropy.

highly anisotropic medium. The δt curve shows similar variation to that seen in model 2. Although similar to model 2, where the magnitude of splitting increases with anisotropic strength rather than increasing path length, there is an observable moveout of the peaks with increasing thickness (Fig. 4). This sensitivity with depth can be used to interpret something about the depth to the anisotropic region. We discuss this further in relation to the MER results in Section 3.1.

2.4 Model class 4: varying frequency of propagating wave

The fourth variable tested is the dominant period of the incoming wave (all other parameters are held constant: rift width = 40 km, maximum *S*-wave anisotropy = 10 per cent, depth of anisotropy = 45 km, initial polarization = 45°). It is evident that varying the dominant period has a large effect on the variation observed in both δt and ϕ (Fig. 5). For higher frequencies the curves match the input model well, with little deviation in δt and a sharp transition in ϕ. The observation that the inflexion points in ϕ describe the width of the rift zone still applies for all frequencies. For higher frequencies the peaks in δt are narrow, an effect of approaching the ray theoretical limit. This shows the importance of investigating shear wave splitting using a finite-frequency approach, where the influence of frequency dependent shear wave coupling is accounted for.

2.5 Model class 5: varying initial polarization of the incoming shear wave

The fifth variable tested is the initial polarization of the incoming wave (all other parameters are held constant: rift width = 40 km,

© 2010 The Authors, *GJI*
Journal compilation © 2010 RAS

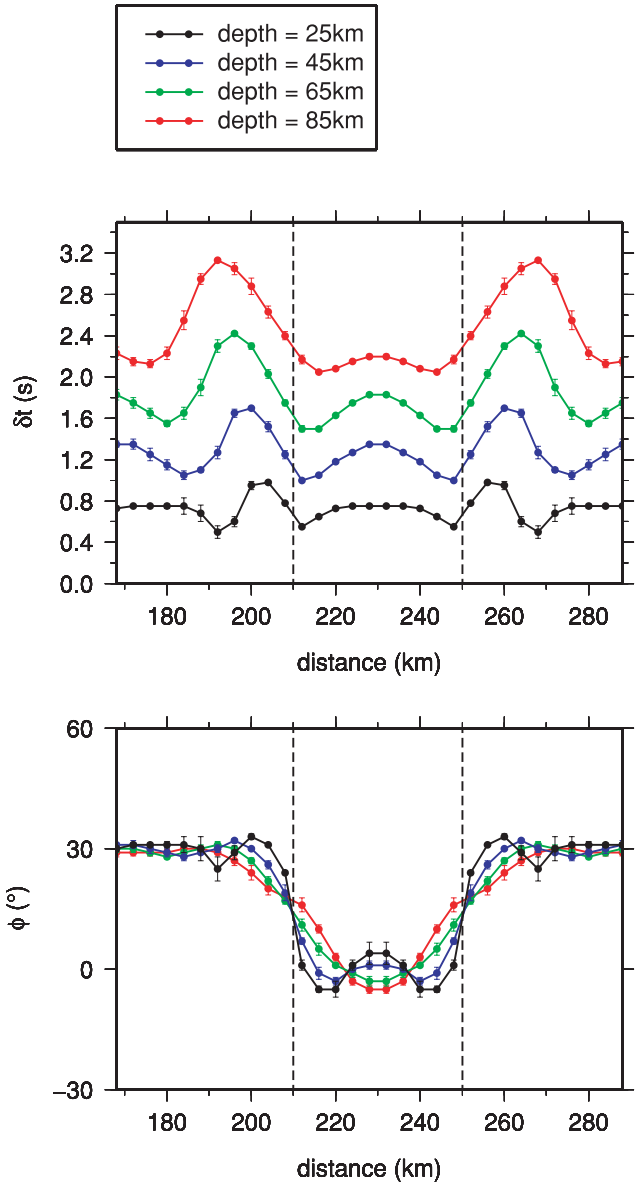

Figure 4. Model 3: varying anisotropic depth. Other parameters: rift width = 40 km, maximum *S*-wave anisotropy = 10 per cent, Period = 8 s, initial polarization = 45°. Black dashed line indicates the rift width for the model. Note similar curves to model 2, but now the peaks and troughs in the δt profile moveout with increasing depth of the anisotropic layer. The flexure points still mark out the rift width, except for the 85 km case where multipathing effects cause a deviation in the ϕ profile.

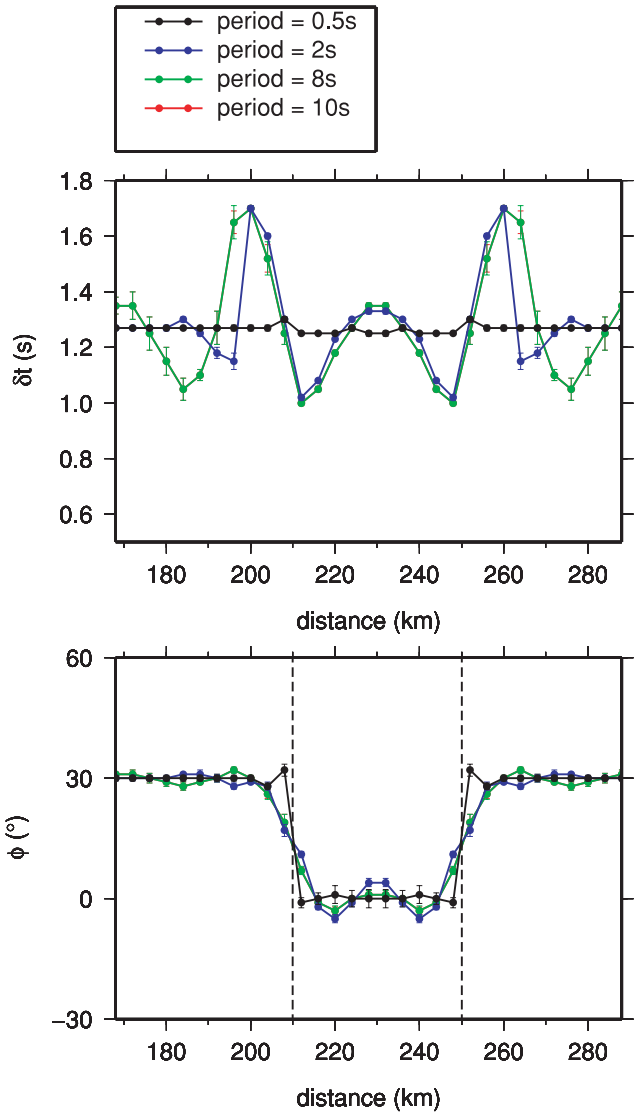

Figure 5. Model 4: varying frequency of incoming wave. Other parameters: rift width = 40 km, maximum *S*-wave anisotropy = 10 per cent, anisotropic depth = 45 km, initial polarization = 45°. Black dashed line indicates the rift width for the model. Note higher frequencies approach a ray based model, and show little deviation from the input model. inflexion points in the ϕ profile still map out the rift width.

maximum *S*-wave anisotropy = 10 per cent, depth of anisotropy = 45 km, dominant period = 8 s). The variation in ϕ is dependent on the initial polarization, but the inflexion points still define the width of the rift zone (Fig. 6). The transition in ϕ from 30° to 0° occurs over distances of ∼20–50 km. It is evident that δt is strongly dependent on the initial polarization, with the peaks in δt occurring either side, and on top of the transition between anisotropic regions (Fig. 6). This is similar to previous studies of inhomogeneous anisotropic structure which show that the measured splitting parameters are highly dependent on the initial polarization of the shear wave (Silver & Savage 1994; Rümpker & Silver 2000; Rümpker *et al.* 2003).

The variation in the δt profile depends on the relationship between the initial polarization and the two anisotropic symmetry axes. For example, model 5 shows that for an initial polarization of 105° the peak in the δt curve lies directly above the transition zone. This initial polarization is oriented 75° from both the 30° fast direction outside the rift, and the 0° inside the rift (105° = −75°). However, when the initial polarization is preferentially close to one of the symmetry axis (assuming it is not so close that a null measurement is recorded), it will induce an asymmetry in the observed δt measurements. This result is consistent with the observation that the finite-frequency sensitivity kernel of the incoming shear wave depends on the initial polarization (Favier & Chevrot 2003; Chevrot *et al.* 2004).

3 DISCUSSION

For all the scenarios modelled in Section 2 it is evident that sharp lateral changes in anisotropic fabric can be detected using shear wave splitting. The sharpness of the transition in splitting parameters

© 2010 The Authors, *GJI*
Journal compilation © 2010 RAS

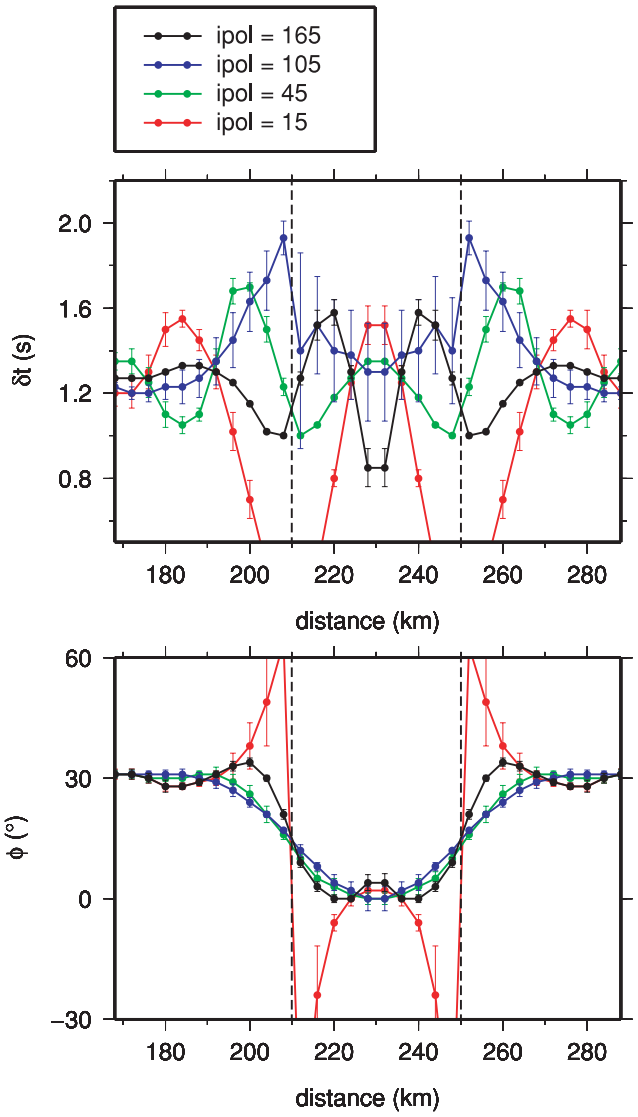

Figure 6. Model 5: Varying initial polarization. Other parameters: rift width = 40 km, maximum *S*-wave anisotropy = 10 per cent, anisotropic depth = 45 km, frequency = 8 s. Black dashed line indicates the rift width for the model. Note a high variability in δt and ϕ profiles with initial polarization.

depends on three parameters, the thickness of the anisotropic layer (Fig. 4), the frequency of the incoming wave (Fig. 5) and the initial polarization of the shear wave (Fig. 6). For example, for an 8 s wave (e.g. *SKS*), the transition in ϕ from 30° to 0° occurs over ∼20 km (25-km-thick layer) to ∼40 km (85-km-thick layer), assuming a constant initial polarization. For a constant thickness of anisotropy (45 km) the transition in ϕ varies from ∼20–50 km, depending on the initial polarization. In all model classes, except where the splitting is very large, the inflexion points in the ϕ curve define the transition in anisotropic fabric. For the MER this will indicate the rift width, but this phenomenon can also potentially be used to determine the location of transform faults and suture zones.

Having constrained the rift width from ϕ it is possible to use the variation in δt to place constraints on the thickness of the anisotropic layer. The position of the peaks and troughs in δt vary for differing rift widths, frequency content of the incoming wave, thickness of the anisotropic layer and initial polarization. By assuming a dominant period of the incoming *SKS*-phase of 8 s, we can use the position of the peaks and troughs to estimate the thickness of the anisotropic layer. This can only be done for one initial polarization (approximately the same as backazimuth for an *SKS* wave).

From studying the variations in ϕ and δt we can estimate the width and thickness of the anomalous anisotropic zone, and from this it is simple to estimate the magnitude of anisotropy. The magnitude of anisotropy is calculated by determining the amount needed to match the splitting results far from the rift. In our models we impose a vertical transition in anisotropic regions. We acknowledge that dipping boundaries may effect these results, and more modelling is need to constrain this.

This modelling exercise has highlighted other features which may be observable in data to detect lateral variations in anisotropy. It is evident that stations close to the transition will show large variation in δt as a function of backazimuth, whereas the same stations will show little variation of ϕ. This is notably different from what is expected from two horizontal layers of splitting, which causes variations in both ϕ and δt (Silver & Savage 1994). Another feature which can be observed is the variation of δt as a function of frequency, again close to the transition in anisotropic domains.

3.1 Comparison with the Main Ethiopian Rift

Kendall *et al.* (2005) observe a rotation in the splitting fast direction inside the MER valley, with the fast shear wave aligning with the magmatic segments (Fig. 7). This pattern could be caused by OMP or along-rift flow, which causes a LPO of olivine. A study of surface waves (Kendall *et al.* 2006; Bastow *et al.* 2010) addresses this ambiguity, due to the azimuthal variations expected for observed phase velocities on interstation paths being different for OMP or LPO. Kendall *et al.* (2006) and Bastow *et al.* (2010) show that to satisfy both the *SKS*-wave splitting results and surface wave results an OMP source of anisotropy, down to depths of at least 70 km, must be present. Keir *et al.* (2005) analysed splitting in shear waves from local earthquakes <20 km beneath the MER, and found fast directions similar to Kendall *et al.* (2005), aligning with the magmatic segments. They also found elevated splitting magnitudes above regions where melt has been inferred from wide-angle refraction (Mackenzie *et al.* 2005) and controlled source tomography (Keranen *et al.* 2004).

Other *SKS*-wave splitting results around Ethiopia show similar results. Ayele *et al.* (2004) observed splitting in Kenya, Ethiopia and Djibouti, and noted that the magnitude of splitting increases with the amount of melt produced, inferred from a correlation between an increase in delay time and volcanism. Gashawbeza *et al.* (2004) performed shear wave splitting on a network of wider aperture, but similar location to Kendall *et al.* (2005). They observed similar rift parallel trends in the fast directions, but argued that fossilized Precambrian anisotropy was the source of this splitting, with some more recent Neogene influence near the rift to explain the rotation in the fast directions.

Melt has been observed beneath the plateau in the form of highly conductive bodies in magneto-telluric surveys (Whaler & Hautot 2006), and underplating is observed in wide-angle reflection profiles (Mackenzie *et al.* 2005). It seems likely that a combination of both pre-existing fabric, and melt induced anisotropy could be present beneath the plateau region. Further evidence of melt beneath the MER comes from receiver function studies. High values of Poisson's ratio >0.3 for the average crust, and underplating highlight the likelihood of melt beneath Afar (Dugda & Nyblade 2006) and the MER (Stuart *et al.* 2006).

© 2010 The Authors, *GJI*
Journal compilation © 2010 RAS

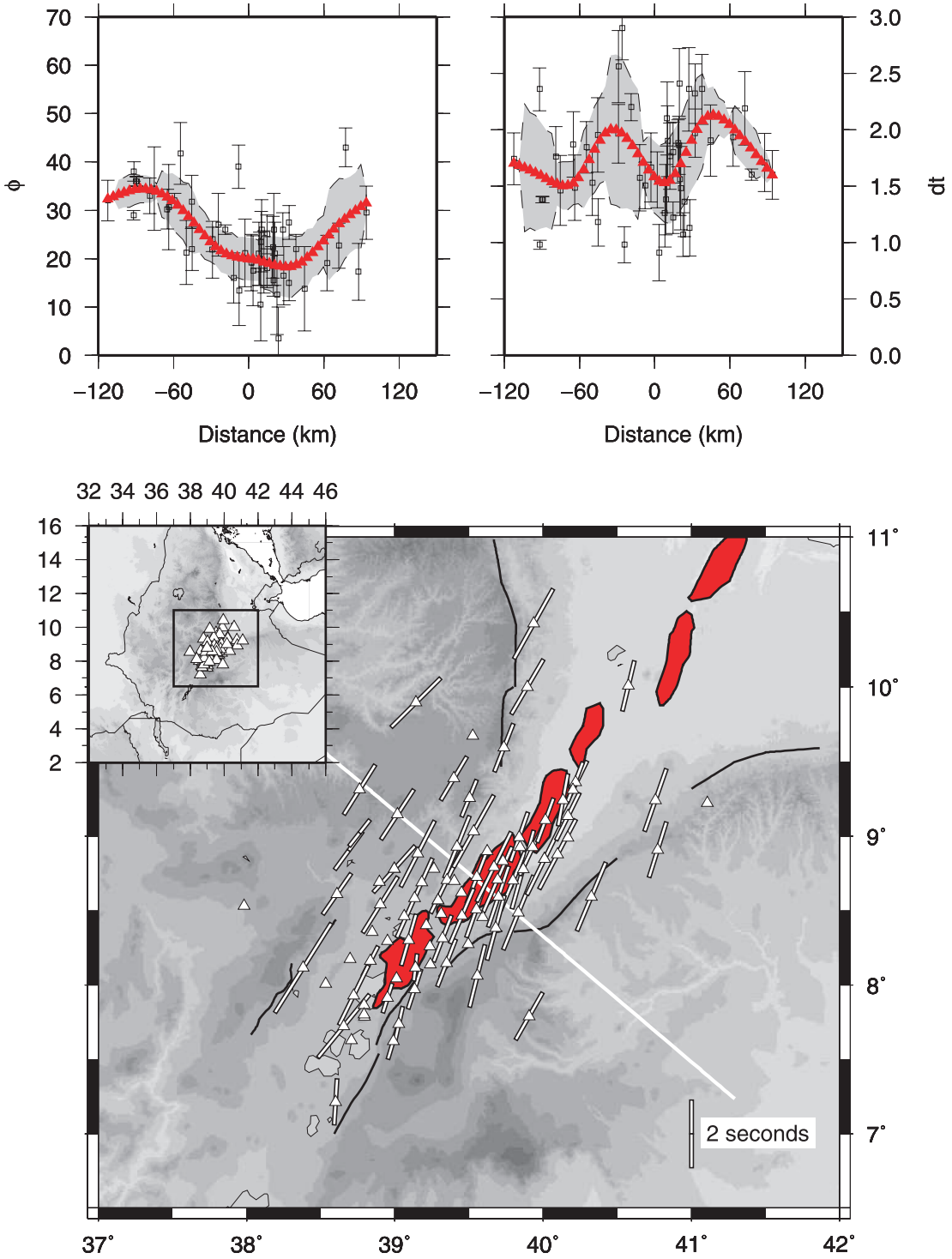

Figure 7. Average *SKS*-wave splitting results beneath the Main Ethiopian Rift (MER), adapted from Kendall *et al.* (2005). The orientation of the white bars shows the fast shear wave direction, and the length is proportional to the amount of splitting. Heavy black lines indicate major border faults and magmatic segments are marked in red. The solid white line perpendicular to the rift indicates the profile used to construct the top panels. The inset plot shows the location of the EAGLE array in Ethiopia. The top panels show shear wave splitting parameters as a function of distance from the rift axis. The red triangles show an interpolated fit to the data using a cubic B-spline interpolation with a knot spacing of 30 km. The shaded region shows the rms misfit of the data from the curve over a 30 km sliding window.

Using the criteria outlined in the previous section we can match the pattern of results observed by Kendall *et al.* (2005) (Fig. 7), and thus place more constraints on melt induced anisotropy beneath the MER.

As was shown in the previous section, the variation of ϕ is relatively insensitive to all parameters (assuming an instantaneous change in anisotropic parameters at the transition), and the observation that the 'rift' width can be defined by the inflexion

© 2010 The Authors, *GJI*
Journal compilation © 2010 RAS

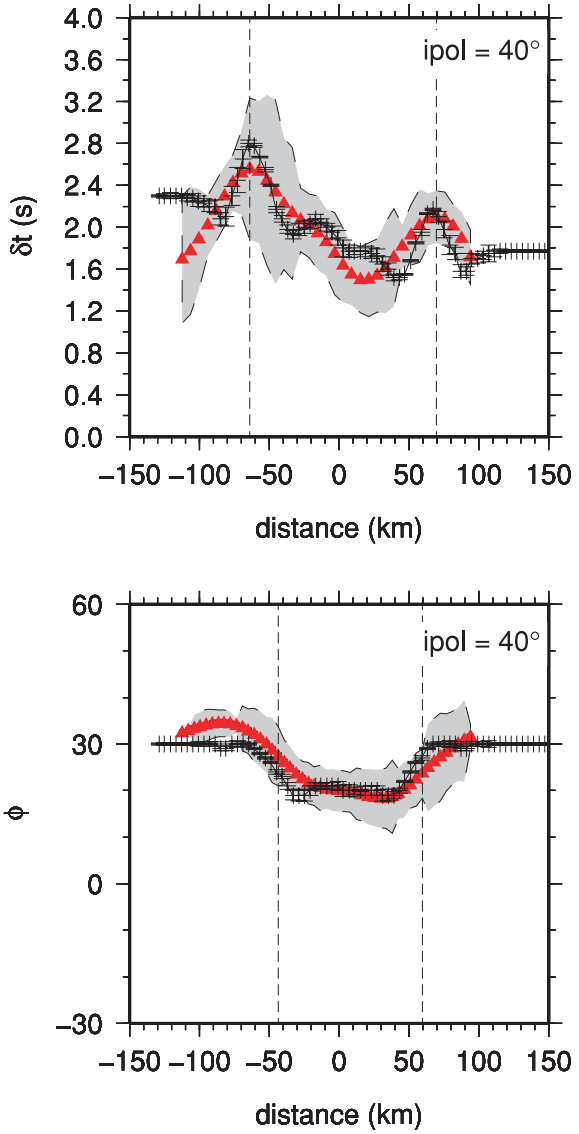

Figure 8. Best-fitting model to the results of Kendall *et al.* (2005). Rift width = 100 km, maximum *S*-wave anisotropy = 9 per cent <−14 km, anisotropy = 7 per cent >−14 km, anisotropic depth = 90 km, frequency = 8 s, initial polarization = 40°. The δt model results are compared to splitting results from one event with a backazimuth of 40°, and the ϕ model results are compared with all splitting results.

points is robust, except in the presence of very high splitting. For the EAGLE data set, this results in a rift width of ∼100 km, based on all the splitting results from different backazimuths, with a fast direction of 30° outside the rift, and 20° inside the rift (Fig. 8).

We have shown that variation in δt is dependent on frequency, initial polarization and vertical thickness of the anisotropic zone. To model this event we take a real SKS waveform from the Ethiopian seismic station ADEE (Fig. 9) (see Bastow *et al.* 2008, for station details), and propagate this through the model. However, an 8 s Ricker wavelet, as used in the previous sections, produces identical results. We cannot use all the data, as we did for measuring the rift width, as they come from differing backazimuths. To account for this we take results from one very well constrained *SKS*-wave splitting event that was recorded across the whole array. This event has a backazimuth of 40°. We run a model, based on this information, to estimate the depth of the anisotropy. The model has a 100 km wide rift zone, 10 per cent anisotropy, a fast direction of 30° outside the rift and 20° inside, an initial polarization of 40° and a period of 8 s (Fig. 10). It is evident that the peaks are moving out with anisotropic thickness, and if we plot the peak–peak width as a function of depth it is evident that they lie on a straightline (Fig. 10). This observation is valid for initial polarizations which fall outside the null planes of either of the anisotropic regions, and outside the null planes for effective splitting parameters observed near the transition between anisotropic regions. For the event with backazimuth of 40° the peak–peak width is 133 km (Fig. 8), which equates to a depth of 90 km. With this information we can estimate the magnitude of anisotropy needed to generate the amount of splitting observed. However, the peaks seen in δt vary in magnitude with the western plateau having elevated shear wave splitting compared to the eastern plateau. As a result we propose a model which has 9 per cent anisotropy on the western plateau and in the westernmost 30 km of the rift zone and 7 per cent anisotropy on the eastern plateau and easternmost 70 km of the rift zone (Fig. 8). Unfortunately, no other events were suitably recorded across the whole array and thus comparisons of this model with splitting results from other backazimuths cannot be performed.

We estimate a region of anisotropy which extends to a depth of ∼90 km beneath the MER, extending beneath the two margins and the rift valley. On the margins the anisotropy is oriented with a fast direction of 30°, and beneath the rift valley the anisotropy is perturbed with an orientation of 20°. The anisotropy below the rift valley correlates with the magmatic segments, as described by Kendall *et al.* (2005). The variation evident in δt can largely be explained as an effect of these two different anisotropic regimes interacting. The variation in δt is highest on the western margin and results in an estimate of 9 per cent anisotropy beneath this region compared to 7 per cent on the eastern margin. This model is summarized in Fig. 11. This model was estimated using a trial and error approach. To fully constrain this model requires a more complete sampling of the whole model space, which is computationally impractical. As a result we cannot formally discuss errors of the fit to the data here. To provide confidence in our models we can compare our results with other geophysical data. To fully explore the model space, studies that invoke theoretical sensitivity kernels may be suitable (Chevrot 2006; Chevrot & Monteiller 2009).

If anisotropy is derived from OMP, as suggested by Kendall *et al.* (2005) then this suggests that melt present beneath the MER is aligned from a depth of 90 km, with an average anisotropy of 7–9 per cent. This equates to a melt fraction of 7–9 per cent, assuming vertically oriented isolated melt inclusions with an aspect ratio of 0.01, but the amount of melt needed to produce this amount of splitting would be smaller for inclusions with a lower aspect ratio.

This estimate of the depth extent of melt induced anisotropy is supported by other studies. Kendall *et al.* (2006) show that azimuthal anisotropy seen in surface wave results occurs at depths between 50 and 70 km, and may extend further but resolution decreases below these depths. Based on simple Fresnel zone estimates, Kendall *et al.* (2005) place the origin of the anisotropy seen in the EAGLE data to be <100 km, a fairly accurate estimate based on these results. *P*- and *S*-wave tomography show the lowest seismic velocities in the top 100 km (Bastow *et al.* 2005, 2008) (Fig. 11) and Ayele *et al.* (2004) image a discontinuity at a depth of ∼90 km which they suggest is the base of the lithosphere. Based on geochemical evidence, Rooney *et al.* (2005) suggest that the base of the lithosphere is the origin of melt generation feeding the MER. Additionally, Keir *et al.*

© 2010 The Authors, *GJI*
Journal compilation © 2010 RAS

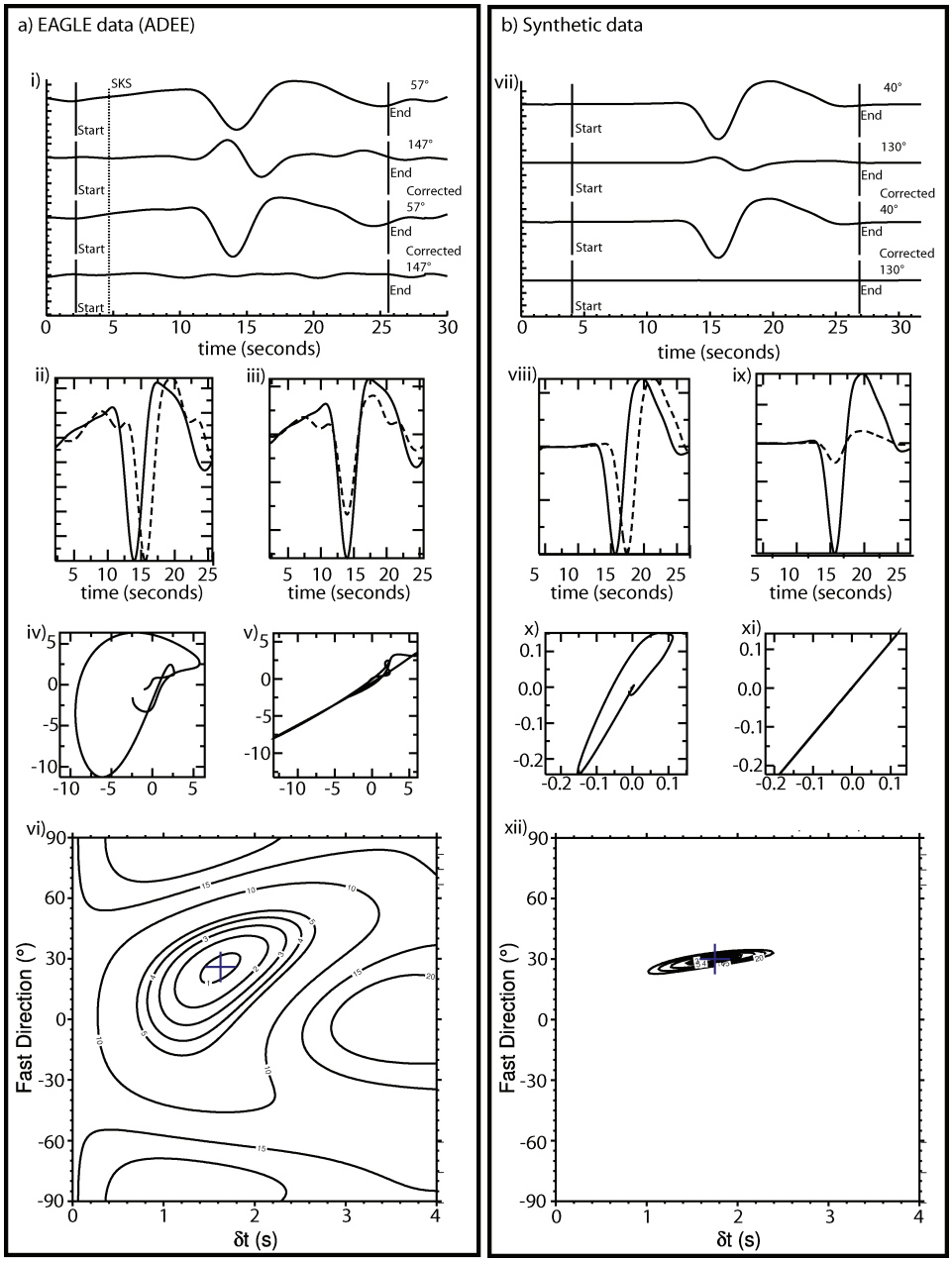

Figure 9. An example of the Teanby *et al.* (2004) method of splitting for (a) EAGLE station ADEE (Event information: 2001 December 2, 13:01:53, 39.40°N, 141.09°E, 123.8 km, M_w 6.5), after Kendall *et al.* (2005). (b) Synthetic data for an MER model (Fig. 9). Both traces are located on the Eastern margin of the rift zone. (i and vii) Traces rotated into R and T directions before and after the anisotropy correction. R component is the initial shear wave polarization before entering the anisotropic region. T component is perpendicular to the R component. Energy on the corrected transverse trace should be minimized in the analysis window. (ii and viii) Uncorrected fast/slow shear waveforms. (iii and ix) Corrected fast/slow shear waveforms. (iv and x) Particle motion for uncorrected seismograms. (v and xi) Particle motion for corrected seismograms. A good result will show similar fast/slow waveforms and any elliptical particle motion will be linearized. (vi and xii) The results of the grid search over δt and ϕ. The method used minimizes the second eigenvalue of the particle motion (i.e. the best result occurs where the particle motion is linear after removing the splitting). The optimum splitting parameters are represented by the cross, and the 1st surrounding contour denotes the 95 per cent confidence interval.

(2009) suggest that partial melting of the lithosphere and subsequent magma injection causes lower crustal earthquakes throughout the MER and western plateau.

Seismic tomography (Bastow *et al.* 2005, 2008) (Fig. 11) and magneto-tellurics (Whaler & Hautot 2006) both show evidence for an asymmetry in melt production, with lower velocities and higher conductivities present beneath the western plateau compared to the eastern plateau. This is supported by our results, which show elevated anisotropy in the west, mainly at the region we define as the rift boundary. Holtzman & Kendall (in review) suggest that melt is concentrated in regions of higher strain, and cite the elevated δt seen by Kendall *et al.* (2005) as evidence for this. We show that an elevated δt can be explained by a simple variation in fast direction alone across the region, but we still require elevated anisotropy close to the western margin, as suggested by Holtzman & Kendall (in review), to explain the asymmetry seen in δt.

© 2010 The Authors, *GJI*
Journal compilation © 2010 RAS

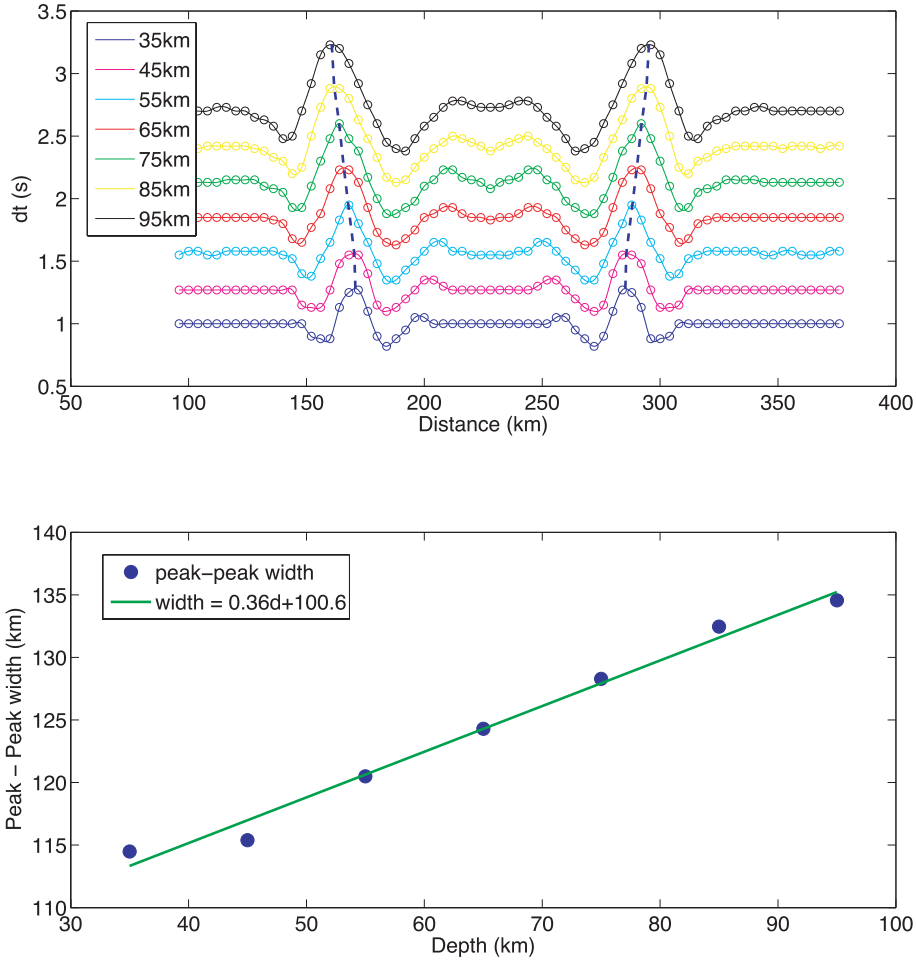

Figure 10. Top panel: variation in δt profile with varying depth extent of anisotropy (similar to model 3). Blue dashed line shows the moveout with depth of the peaks in the δt profile. Bottom panel: least-squares fit to the location of the peaks in the δt profile with depth. Model parameters used in this model are rift width = 100 km, maximum *S*-wave anisotropy = 10 per cent, variable anisotropic depth, frequency = 8 s, initial polarization = 40°.

4 CONCLUSIONS

We have developed a modelling technique, using a one-way wave equation approach, to investigate the effects of laterally varying anisotropy on shear wave splitting. We have shown that:

(i) *SKS*-wave splitting can be used to identify changes in fast direction over lateral distances of 20–50 km (dependent on depth and initial polarization).

(ii) The inflexion points in the ϕ profile demarcate the transition in anisotropy.

(iii) Variation in the position of the peaks and troughs seen in δt depend on anisotropic thickness from the surface, and for a given initial polarization can be used to place depth constraints on the anisotropic region.

(iv) With information on the depth of the anisotropic region, estimates can be placed on the percentage of anisotropy in the region.

(v) At stations close to the transition δt varies as a function of backazimuth and frequency, whereas ϕ shows little such variation. This can be used as an indicator of lateral changes in anisotropy

(vi) For higher frequencies the modelled splitting approaches the ray theoretical limit, and shows little variation in δt. Thus, a frequency dependence of δt could indicate a lateral transition in anisotropy. This also shows the importance of performing finite frequency waveform modelling as opposed to ray-based approaches in regions where anisotropy varies over length scales comparable to the dominant seismic wavelength.

Determining the exact cause and symmetry of the anisotropy still requires analysis of other phases [e.g. joint shear wave splitting and surface waves Brisbourne *et al.* (1999), Kendall *et al.* (2006)]. However, we show that a simple rotation in the anisotropic characteristics in a 100 km wide 'rift' zone can explain much of the variation seen in the Kendall *et al.* (2005) MER splitting results. The anisotropy across the model is confined to the uppermost 90 km. This region of anisotropy coincides with regions with low velocities (Bastow *et al.* 2008), high anisotropy (Kendall *et al.* 2006), high conductivities (Whaler & Hautot 2006), and the suggested base of the lithosphere (Ayele *et al.* 2004). It has also been suggested that this region is where melt is generated that feeds the MER (Rooney *et al.* 2005). However, a simple rotation alone is not enough to reproduce these results. We require elevated anisotropy at the western margin to match the higher δt seen in the splitting results in this region. This coincides with the lowest velocities (Bastow *et al.* 2008) (Fig. 11), highest conductivities (Whaler & Hautot 2006) and regions of magmatic underplate (Mackenzie *et al.* 2005; Cornwell *et al.* 2006). Holtzman & Kendall suggested that the elevated splitting is caused

© 2010 The Authors, *GJI*
Journal compilation © 2010 RAS

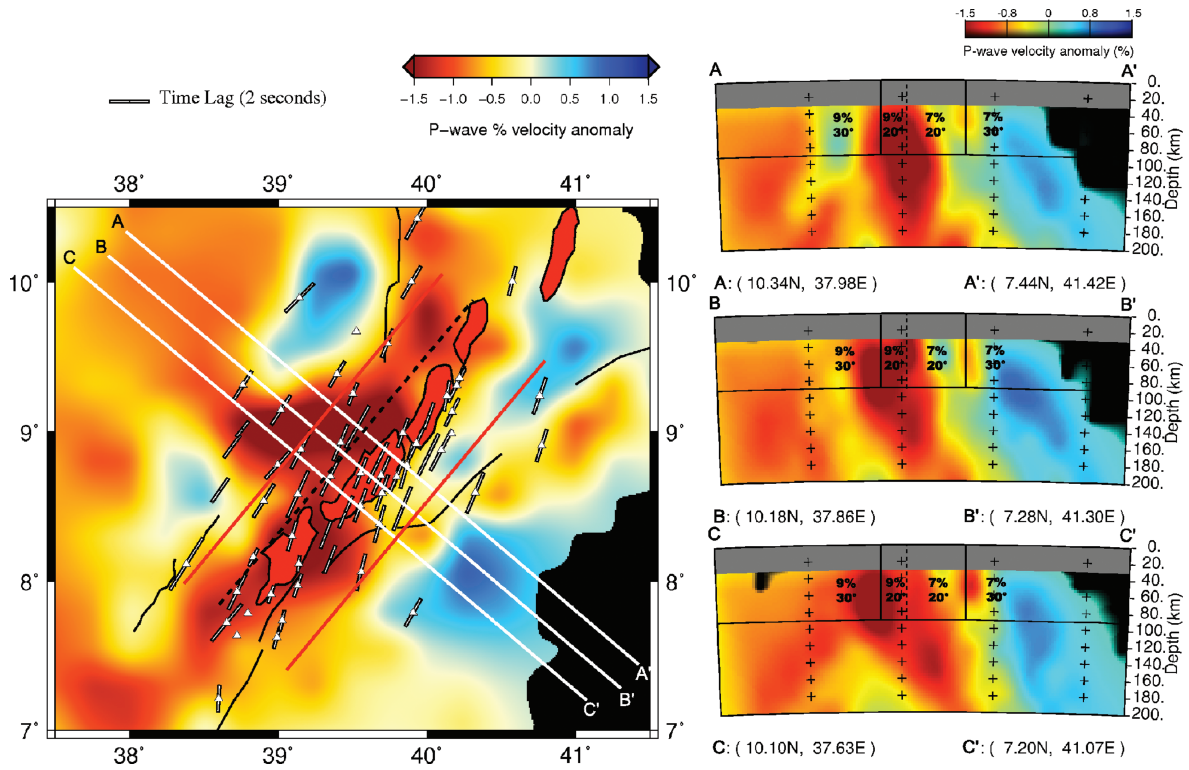

Figure 11. Map (left-hand panel) and cross-section (right-hand panel) view of the best-fitting model from Fig. 9, plotted over the *P*-wave tomographic images of Bastow *et al.* (2008). The red lines on the left plot highlight the modelled rift edges, and the dashed black line indicates the transition from 9 per cent anisotropy to 7 per cent. The white lines indicate the location of the tomographic cross-sections. There is a strong correlation between the slow velocity anomalies and the regions of 9 per cent anisotropy. Also the slowest anomalies appear to be present in the top 100 km, similar to where we constrain the anisotropy to be.

by focused melt along the margin, where strain is highest. The elevated anisotropy on the western margin required by our models supports this, with little effect seen on the eastern margin where smaller evidence of melt related phenomena are observed. These results show how observations of seismic anisotropy provides insights into the role of magma in rifting.

ACKNOWLEDGMENTS

We thank all involved in the EAGLE project and IRIS for providing the data set. We also thank Ian Bastow for providing his tomography models, and for useful discussion. Two anonymous reviews are thanked for thoughtful comments which helped improve the paper. This project is funded by NERC (grant no: NE/E005284/1), as part of the Afar Rift Consortium project.

REFERENCES

Alsina, D. & Snieder, R., 1995. Small-scale sublithospheric continental mantle deformation—constraints form SKS splitting observations, *Geophys. J. Int.,* **123,** 431–448.

Angus, D.A. & Thomson, C.J., 2006. Numerical analysis of a narrow-angle, one-way, elastic-wave equation and extension to curvilinear coordinates, *Geophysics,* **71**(5), 137–146.

Angus, D.A., Thomson, C.J. & Pratt, R.G., 2004. A one-way wave equation for modelling seismic waveform variations due to elastic anisotropy, *Geophys. J. Int.,* **156,** 595–614.

Ayele, A., Stuart, G. & Kendall, J., 2004. Insights into rifting from shear wave splitting and receiver functions: an example from Ethiopia, *Geophys. J. Int.,* **157**(1), 354–362.

Babuska, V. & Cara, M., 1991. *Seismic Anisotropy in the Earth*, Kluwer Acad., Norwell, Mass.

Bastow, I.D., Stuart, G.W., Kendall, J.-M. & Ebinger, C.J., 2005. Upper-mantle seismic structure in a region of incipient continental breakup: northern Ethiopian rift, *Geophys. J. Int.,* **162,** 479–493.

Bastow, I.D., Nyblade, A.A., Stuart, G.W., Rooney, T.O. & Benoit, M.H., 2008. Upper mantle seismic structure beneath the Ethiopian hot spot: rifting at the edge of the African low-velocity anomaly, *Geochem. Geophys. Geosyst.,* **9**(12), Q12022, doi:10.1029/2008GC002107.

Bastow, I., Pilidou, S., Kendall, J.-M. & Stuart, G., 2010. Melt-induced seismic anisotropy and magma assisted rifting in Ethiopia: evidence from surface waves, *Geochem. Geophys. Geosyst.*, in press.

Behn, M.D., Conrad, C.P. & Silver, P.G., 2004. Detection of upper mantle flow associated with the African Superplume, *Earth planet. Sci. Lett.,* **224**(3–4), 259–274.

Blackman, D.K. & Kendall, J.-M., 1997. Sensitivity of teleseismic body waves to mineral texture and melt in the mantle beneath a mid-ocean ridge, *Phil. Trans. R. Soc. Lond. A,* **355,** 217–231.

Blackman, D.K. & Kendall, J.-M., 2002. Seismic anisotropy in the upper mantle 2. Predictions for current plate boundary flow models, *Geochem. Geophys. Geosyst.,* **3**(9), 8602, doi:10.1029/2001GC000247.

Brisbourne, A., Stuart, G. & Kendall, J.-M., 1999. Anisotropic structure of the Hikurangi subduction zone, New Zealand-integrated interpretation of surface-wave andbody-wave observations, *Geophys. J. Int.,* **137**(1), 214–230.

Chevrot, S., 2006. Finite-frequency vectorial tomography: a new method for high-resolution imaging of upper mantle anisotropy, *Geophys. J. Int.,* **165,** 641–657.

Chevrot, S. & Monteiller, V., 2009. Principles of vectorial tomography—the effects of model parametrization and regularization in tomographic imaging of seismic anisotropy, *Geophys. J. Int.,* **179,** 1726–1736.

© 2010 The Authors, *GJI*
Journal compilation © 2010 RAS

Chevrot, S., Favier, N. & Komatitsch, D., 2004. Shear wave splitting in three-dimensional anisotropic media, *Geophys. J. Int.,* **159,** 711–720.

Cornwell, D.G., Mackenzie, G.D., England, R.W., Maguire, P.K.H., Asfaw, L.M. & Oluma, B., 2006. Northern Main Ethiopian Rift crustal structure from new high-precision gravity data, in*The Afar Volcanic Province within the East African Rift System no*,. **259,** pp. 307–321, eds Yirgu, G., Ebinger, C.J. & Maguire, P.K.H., Geological Society, Special Publication, London, UK.

Crampin, S. & Booth, D.C., 1985. Shear-wave polarizations near the North Anatolian Fault, II: interpretation in terms of crack-induced anisotropy, *Geophys. J. R. astr. Soc.,* **83,** 75–92.

Crampin, S. & Yedlin, M., 1981. Shear-wave singularities of wave propagation in anisotropic media, *J. Geophys.,* **49,** 43–46.

Dugda, M.T. & Nyblade, A.A., 2006. New constraints on crustal structure in eastern Afar from the analysis of receiver functions and surface wave dispersion in Djibouti, in *The Afar volcanic Province within the East African Rift System no*,. **259,** pp. 55–72, eds Yirgu, G., Ebinger, C.J. & Maguire, P.K.H., Geological Society,Special Publication, London, UK.

Favier, N. & Chevrot, S., 2003. Sensitivity kernels for shear wave splitting in transverse isotropic media, *Geophys. J. Int.,* **153**(1), 213–228.

Gashawbeza, E.M., Klemperer, S.L., Nyblade, A.A., Walker, K.T. & Keranen, K.M., 2004. Shear-wave splitting in Ethiopia: Precambrian mantle anisotropy locally modified by Neogene rifting, *Geophys. Res. Lett.,* **31,** doi:10.1029/2004GL020471.

Holtzman B.K. & Kendall, J.-M., in review. Organized melt, seismic anisotropy and plate boundary lubrication, *Geochem. Geophys. Geosyst.*, in press.

Hudson, J., 1981. Wave speeds and attenuation of elastic waves in material containing cracks, *Geophys. J. Int.,* **64**(1), 133–150.

Keir, D., Kendall, J.-M., Ebinger, C.J. & Stuart, G.W., 2005. Variations in late syn-rift melt alignment inferred from shear-wave splitting in crustal earthquakes beneath the Ethiopian rift, *Geophys. Res. Lett.,* **32,** doi:10.1029/2005GL024150.

Keir, D., Bastow, I.D., Whaler, K.A., Daly, E., Cornwell, D.G. & Hautot, S., 2009. Lower crustal earthquakes near the Ethiopian rift induced by magmatic processes, *Geochem. Geophys. Geosyst.,* **10,** Q0AB02, doi:10.1029/2009GC002382.

Kendall, J.-M., 1994. Teleseismic arrivals at a mid-ocean ridge: effects of mantle melt and anisotropy, *Geophys. Res. Lett,* **21**(4), 301–304.

Kendall, J.-M., 2000. Seismic anisotropy in the boundary layers of the mantle, in *Earth's Deep Interior: Mineral Physics and Tomography From the Atomic to the Global Scale*, no. **117,** pp. 133–159, eds Karato, S., Forte, A.M., Liebermann, R.C., Masters, G. & Stixrude, L., Geophysical Monograph.

Kendall, J.-M., Stuart, G.W., Ebinger, C.J., Bastow, I.D. & Keir, D., 2005. Magma-assisted rifting in Ethiopia, *Nature,* **433**(7022), 146–148.

Kendall, J.-M., Pilidou, S., Keir, D., Bastow, I.D., Stuart, G.W. & Ayele, A., 2006. Mantle upwellings, melt migration and the rifting of Africa: Insights from seismic anisotropy, in *The Afar Volcanic Province within the East African Rift System*, no. **259,** pp. 55–72, eds Yirgu, G., Ebinger, C.J. & Maguire, P.K.H., Geological Society, Special Publication, London, UK.

Keranen, K., Klemperer, S.L., Gloaguen, R. & Group, E.W., 2004. Three-dimensional seismic imaging of a protoridge axis in the Main Ethiopian rift, *Geology,* **32**(11), 949–952.

Mackenzie, G.D., Thybo, H. & Maguire, P.K.H., 2005. Crustal velocity structure across the Main Ethiopian Rift: results from two-dimensional wide-angle seismic modelling, *Geophys. J. Int.,* **162**(3), 994–1006.

Mainprice, D., Barruol, G. & Ben Ismail, W., 2000. The seismic anisotropy of the Earth's mantle: from single crystal to polycrystal, in *Earth's Deep Interior: Mineral Physics and Tomography From the Atomic to the Global Scale*, no. **117,** pp. 237–264, eds Karato, S., Forte, A.M., Liebermann, R.C., Masters, G. & Stixrude, L., Geophysical Monograph, AGU, Washington DC.

Rooney, T., Furman, T., Yirgu, G. & Ayalew, D., 2005. Structure of the Ethiopian lithosphere: Xenolith evidence in the Main Ethiopian Rift, *Geochim. Cosmochim. Acta,* **69**(15), 3889–3910.

Rümpker,G. & Ryberg, T., 2000. New 'Fresnel-zone' estimates for shear-wave splitting observations from finite-difference modeling, *Geophys. Res. Lett.,* **27**(13), 2005–2008.

Rümpker, G. & Silver, P.G., 2000. Calculating splitting parameters for plume-type anisotropic structures of the upper mantle, *Geophys. J. Int.,* **143,** 507–520.

Rümpker, G., Ryberg, T., Bock, G. & Desert Seismology Group, 2003. Boundary-layer mantle flow under the Dead Sea transform fault inferred from seismic anisotropy, *Nature,* **425,** 497–501.

Savage, M.K., 1999. Seismic anisotropy and mantle deformation: what have we learned from shear wave splitting? *Rev. Geophys.,* **37**(1), 65–106.

Silver, P.G., 1996. Seismic anisotropy beneath the continents: probing the depths of geology, *Annu. Rev. Earth planet. Sci,* **24,** 385–432.

Silver, P.G. & Chan, W.W.J., 1991. Shear-wave splitting and subcontinental mantle deformation, *J. geophys. Res.,* **96,** 16429–16454.

Silver, P.G. & Savage, M.K., 1994. The interpretation of shear wave splitting parameters in the presence of two anisotropic layers, *Geophys. J. Int.,* **119,** 949–963.

Stuart, G.W., Bastow, I.D. & Ebinger, C.J., 2006. Crustal structure of the northern Main Ethiopian Rift from receiver function studies, in *The Afar Volcanic Province within the East African Rift System*, no. **59,** pp. 55–72, eds Yirgu, G., Ebinger, C.J. & Maguire, P.K.H., Geological Society, Special Publication, London, UK.

Teanby, N.A., Kendall, J.-M. & Van der Baan, M., 2004. Automation of shear-wave splitting measurements using cluster analysis, *Bull. Seis. Soc. Am.,* **94**(2), 453–463.

Whaler, K.A. & Hautot, S., 2006. The electrical resistivity structure of the crust beneath the northern Main Ethiopian Rift, in *The Afar Volcanic Province within the East African Rift System*, no. **259,** pp. 55–72, eds Yirgu, G., Ebinger, C.J. & Maguire, P.K.H., Geological Society, Special Publication, London, UK.

© 2010 The Authors, *GJI*
Journal compilation © 2010 RAS